

Materials Science and Engineering

**Donald R. Lesuer,
Thrust Area Leader**

This is an informal report intended primarily for internal or limited external distribution. The opinions and conclusions stated are those of the author and may or may not be those of the Laboratory.

Work performed under the auspices of the U.S. Department of Energy by Lawrence Livermore National Laboratory under Contract W-7405-Eng-48.

February 1997

Disclaimer

This document was prepared as an account of work sponsored by an agency of the United States Government. Neither the United States Government nor the University of California nor any of their employees, makes any warranty, express or implied, or assumes any legal liability or responsibility for the accuracy, completeness, or usefulness of any information, apparatus, product, or process disclosed, or represents that its use would not infringe privately owned rights. Reference herein to any specific commercial products, process, or service by trade name, trademark, manufacturer, or otherwise does not necessarily constitute or imply its endorsement, recommendation, or favoring by the United States Government or the University of California. The views and opinions of authors expressed herein do not necessarily state or reflect those of the United States Government or the University of California, and shall not be used for advertising or product endorsement purposes.

This report has been reproduced
directly from the best available copy.

Available to DOE and DOE contractors from the
Office of Scientific and Technical Information
P.O. Box 62, Oak Ridge, TN 37831
Prices available from (615) 576-8401, FTS 626-8401

Available to the public from the
National Technical Information Service
U.S. Department of Commerce
5285 Port Royal Rd.,
Springfield, VA 22161

THRUST AREA REPORT • UCRL-ID-125474

Materials Science and Engineering

**Donald R. Lesuer,
Thrust Area Leader**

Reprinted from Engineering Research, Development and Technology
FY 96 UCRL 53868-96

February 1997



Donald R. Lesuer, Thrust Area Leader

During FY-96, work within the Materials Science and Engineering thrust area was focused on material modeling. Our motivation for this work is to develop the capability to study the structural response of materials as well as materials processing. These capabilities have been applied to a broad range of problems, in support of many programs at Lawrence Livermore National Laboratory.

Recent examples of structural response problems studied are material fracture (including interface failure); damage in laser optics; the response of weapons components (including HE); and the failure of composite materials. For materials processing, typical problems studied include metal forming, laser processing, casting and heat treating.

To improve our ability to model material behavior, much of our work involves developing new material models and failure models, and applying the codes to new problems. Most investigations involve experimental studies to gather basic information on material response and to validate codes or material models. Projects are inherently multi-disciplinary, involving several investigators with expertise in materials and mechanics.

In addition to material modeling, the thrust area is also actively involved in superplastic materials and composite materials. Our technology base in these areas is being maintained or, in some cases, expanded through on-going programmatic work.

Superplastic materials are crystalline solids that can be deformed in tension to very large strains with low flow stress. We are currently working on several projects involving superplastic aluminum alloys and superplastic (net shape) forming with institutes in the Former Soviet Union. Our projects have industrial partners in the U.S. and we are developing these technologies for commercial applications.

Work in composite materials has involved metal and polymer matrix composites as well as laminated metal composites. Much of this work involves the use of these materials for lightweight applications.

Our thrust area studies for FY-96 are described in the following five articles: (1) Strength and Fracture Toughness of Material Interfaces; (2) Damage Evolution in Fiber Composite Materials; (3) Flashlamp Envelope Optical Properties and Failure Analysis; (4) Synthesis and Processing of Nanocrystalline Hydroxapatite; and (5) Room Temperature Creep Compliance of Bulk Kel-F.



Materials Science and Engineering

5

5. Materials Science and Engineering

Overview

Donald R. Lesuer, Thrust Area Leader

Strength and Fracture Toughness of Material Interfaces

Robert A. Riddle and David S. Hiromoto5-1

Damage Evolution in Fiber Composite Materials

*Steve J. DeTeresa, Scott E. Groves, Dennis C. Freeman, Patrick J. Harwood,
Roberto J. Sanchez, Marvin A. Zocher, and Edward Zywicz5-5*

Flashlamp Envelope Optical Properties and Failure Analysis

Mark A. Havstad.....5-11

Synthesis and Processing of Nanocrystalline Hydroxyapatite

T. G. Nieh and Donald R. Lesuer.....5-17

Room Temperature Creep Compliance of Bulk Kel-F

Marvin A. Zocher, Steve J. DeTeresa, and Scott E. Groves5-21

Strength and Fracture Toughness of Material Interfaces

Robert A. Riddle and David S. Hiromoto
*Manufacturing and Materials Engineering Division
Mechanical Engineering*

In this project, we have specified desired material properties and created material combinations which in a component will have the required density, stiffness, strength, fracture toughness, manufacturability and cost for a particular application. We are concerned with the effect of processing parameters on the interface strength and interface fracture toughness between ceramic materials and ductile metals. This has lent insight into the macroscopic strength and fracture toughness properties of a metal matrix composite (MMC). We have measured the strength and fracture toughness of aluminum/alumina interfaces on specimens produced by vacuum liquid phase bonding methods, and compared the results to specimens prepared by ultrahigh vacuum diffusion bonding in previous years. We have also developed J Integral methods for quantifying the energy release rates for crack growth at ductile material/ceramic interfaces. As postulated from the test results, the energy-release rate as voids propagate as cracks and then blunt, leads to fairly unique failure behavior.

Introduction

The ductility of the metal phase plays an important role in increasing the fracture toughness of an MMC, while the ceramic particles increase the stiffness and strength. The interface under study here is between aluminum and alumina, both single crystal (sapphire) and polycrystalline. This study is intended to increase our understanding of commercial MMC materials, particularly those that consist of an aluminum alloy reinforced with Al_2O_3 .

MMCs, when properly designed and fabricated, show superior properties, such as increased specific stiffness, reduced coefficient of thermal expansion, improved creep and wear parameters, and reduced fatigue damage at elevated temperatures. To take advantage of these improved properties in component designs, these properties must be both demonstrable and predictable in terms of their fabrication and use history. The production of MMC parts must also be cost-effective. Hence, fundamental understanding of the composition/structure and property/performance relations is required for these composites. A key ingredient in this understanding is the strength and toughness of the interface between the constituent materials.

Progress

We have used the microextensometer system developed in FY-95 to measure the elastic/plastic response of the ductile metal layer in the alumina/aluminum bend bar, tensile, and fracture toughness specimens. In this test system, two cylindrical rods are attached near the ductile layer interface. As the specimens are loaded in the test frame, the distance between the rods increases and a laser measures the increased spacing. The output of the load cell, the cross-head displacement, and the extension of the rod spacing is stored digitally in a computer system. This microextensometer system allows us to measure the constitutive response of thin layers of bonded materials loaded in tension.

We have updated a J Integral post-processor to calculate the energy-release rate available for crack advance at the metal/ceramic interface. This post-processor works in conjunction with a tie-break slide-line to simulate progressive failure at the interface.

Two key areas for the finite element modeling of the failure processes in the MMC include the appropriate failure criteria at the interface, and a straightforward experimental method to measure the failure parameters. The strength of an interface is

measured based on an average stress with no defect present, while the fracture toughness relates to the stress field at a defect, as a function of the defect or crack length. In the modeling of failure at interfaces, a unified failure criterion is sought which combines the stress and strain field at the interface with a critical deformation parameter to describe decohesion of cracked and uncracked interfaces.

Experimental Results

Polycrystalline alumina materials were joined via aluminum foil in a vacuum brazing process. The alumina parts were Coors Ceramics AD-995, which is nominally 99.5% Al₂O₃. The finish of the alumina

bonding surfaces was polished. This best possible finish had a surface roughness that was measured at 5.1 μm peak-to-valley over 5.08 mm. The surfaces were cleaned with acetone, and then rinsed and wiped dry.

The aluminum foil was 99.997% pure aluminum, obtained from Alfa AESAR Puratronic. The foils were 0.05 mm thick.

The assembly of the alumina parts for the four point-bend specimens, with the aluminum foil as the braze medium, into a bonding fixture is shown in **Fig. 1**. The parts and the fixture were placed in a closed chamber, which was evacuated to 1.0 × 10⁻⁶ Torr, then heated to 1200 °C. The temperature was increased to this maximum over the period of 1 h.

In general, the lower temperatures produced poorer bonds. The smaller bend and tensile samples also were better bonded than the larger compact tension samples, suggesting an effect of surface roughness and foil thickness on the bond strength. Some tensile samples were notched to constrain failure to the bond region.

Because of the very small gauge length on the specimens, it was necessary to attach the cylindrical rods on the edge of the specimens, and use the displacement between the rods, as measured by a laser system, to characterize the load versus displacement behavior of the interface braze material.

Of the four bend specimens tested, two failed in the braze joint at an average load of 2544 N. Using the bend beam formula for stress, we calculate a maximum tensile stress of 345 MPa. The specimens

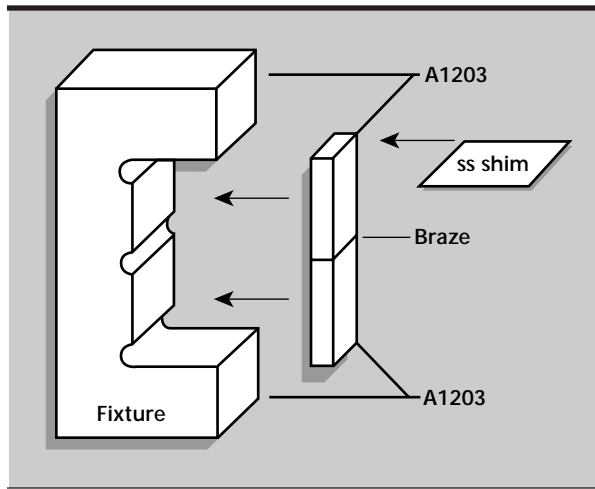
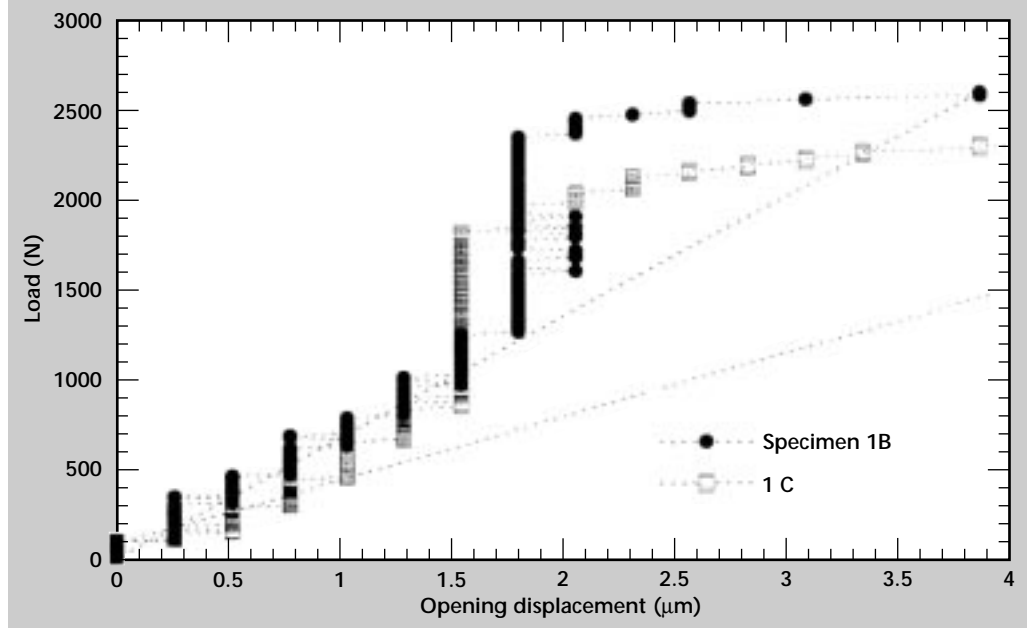


Figure 1. Part assembly for vacuum braze joining the alumina blocks and the aluminum foil.

Figure 2. Load vs opening displacement for bend specimens.



that did not fail at the braze failed at an average 7% higher load. These numbers compare favorably with the typical flexural strength listed in the Coors company sales literature as 379 MPa. The bonds were successful in the sense that they delivered a strength very nearly equal to a typical strength of the substrate material.

These bonds strengths are somewhat larger than values obtained under the previous conditions of ultrahigh vacuum diffusion bonding.¹

Figure 2 shows the displacement characteristics for the two bend specimens that failed in the bond. The significant non-linear deformation prior to final fracture suggests that damage in the form of voids or cracks is present at fairly low loads.² The fact that the load versus displacement curves stiffen in the mid-load region is a distinct characteristic of the specimen failure, and will be investigated further in the analysis section.

Analytical Results

Finite element calculations were performed to derive material failure properties from the bend specimen tests. **Table 1** shows the stress/strain relation for the alumina and aluminum materials.

A mesh of 2632 elements was created to represent the geometry of the alumina/aluminum interface. To get more definition of plastic deformation in the aluminum bond layer, eight elements were used to model its thickness in the region of crack initiation. One eighth the thickness of the bond layer is the smallest geometric feature of the finite element mesh, and controlled the creation of the rest of the mesh, based on limitations of element aspect ratios.

The alumina regions of the bend specimen were modeled to the extent where the inside edge of the cylindrical rods in the microextensometer displacement system would be present in the bend specimens. The right hand or lower side of the mesh was constrained to have zero normal displacement. The left hand or upper side of the mesh had a linearly varying pressure boundary condition, based on the stress distribution predicted in the simple beam theory calculations of stress in the bend specimens. The displacements on the upper edge of the mesh from the finite element calculations are meant to be directly comparable to the displacements measured at the cylindrical rods.

A tie-break slideline was introduced at the interface between the lower edge of the aluminum bond layer and the alumina. The operating features of this slideline are such that until a specified, critical effective plastic strain is reached in the elements

along the slideline, the nodes across the slideline remain tied, representing a bonded region. When the critical effective plastic strain is reached, the slideline opens, the nodal constraints are released, and void growth or crack growth is then simulated.

The crack growth and/or voids at the interface affect the displacements at the boundary edges as the stress is applied, and correspond to the measured loads and displacement, or compliance, as measured in the microextensometer system. A change in specimen compliance is the only measure of defect growth in these experiments.

By doing finite element calculations on several failure scenarios for the bondline, including starting with no crack and no slideline, with a crack, with no crack and a slideline, and with a debond and a slideline, it became clear that the failure scenario with an initial debond, or void, and a tie-break slideline best matched the data produced in the actual tests.

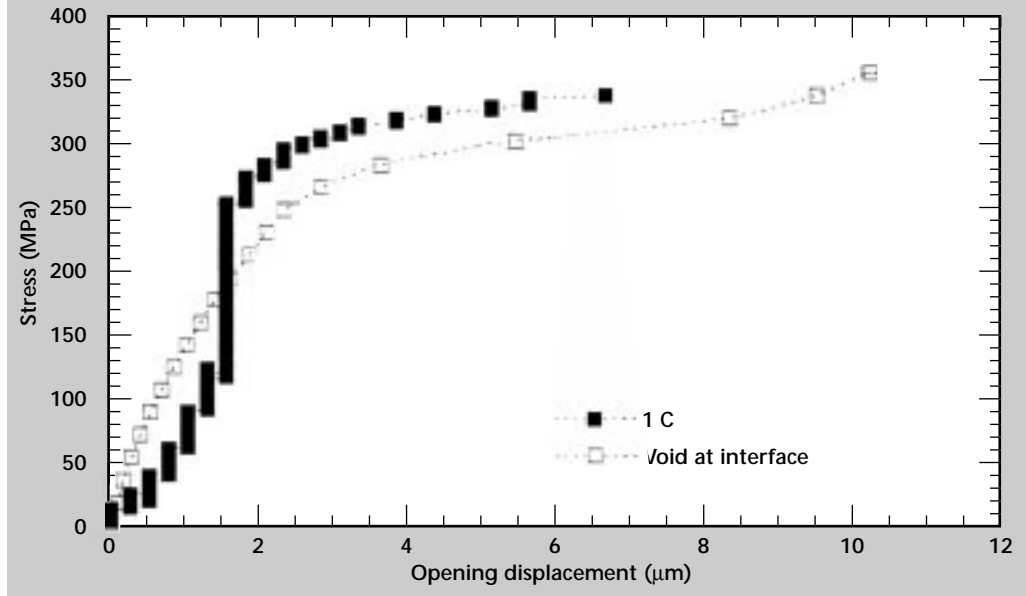
Figure 3 shows the results of a finite element analysis, shown in the open square symbols, of a mesh with an initial debond of 83 μm at the aluminum/alumina interface, centered at 250 μm from the tensile edge of the bend specimen. The agreement is well within the tolerances of the displacement measuring system, and our knowledge of the material properties, such as the modulus of the alumina.

The initial debond grew into a lenticular-shaped void as observed,² and then propagated along the tie-break slideline, with the critical effective plastic strain to failure in the aluminum material being 0.10.

Table 1. Constitutive properties of aluminum and alumina.

Aluminum	
E	$68.942 \times 10^9 \text{ Pa}$
ν	0.33
Stress (Pa)	Strain
3.50×10^6	0.0
1.22×10^7	0.002
1.65×10^7	0.005
2.40×10^7	0.0150
3.44×10^7	0.045
4.85×10^7	0.125
6.85×10^7	0.35
9.74×10^7	1.0
Alumina	
E	$345.0 \times 10^9 \text{ Pa}$
ν	0.21

Figure 3. Stress vs opening displacement for bend specimen calculations.



J Integral calculations for the energy-release rate at the first increment of crack growth yielded 430 Nm/m^2 as the fracture toughness of the interface.

Conclusion

The experimental techniques developed in these efforts to investigate the failure at metal/ceramic interfaces have produced new and interesting results regarding the growth of voids as a precursor to crack growth in the failure at the interface, and the implications on the compliance of specimens with initial debonds as failure proceeds. The development of the microextensometer system was essential in measuring specimen compliances on such a small scale.

Future Work

The analytical techniques, including the development of a more powerful J Integral post-processor, and its correlation with a tie-break slideline in predicting failure at interfaces, should allow application to a wide range of other problems where failure prediction is required.

The analytical and experimental techniques developed in the completion of this project may have a major beneficial effect on several on-going technology transfer projects, particularly efforts with GM

on whisker reinforcement and with ALCOA and Pratt and Whitney on metal laminates. These techniques should also find use in predicting the reliability of interfaces between both metal and ceramics and metal and metals, of importance in the ADaPT program which is to ensure the safety and reliability of the nuclear weapons stockpile into the next century.

Acknowledgments

L. Wagner of Lawrence Livermore National Laboratory's Chemistry and Materials Science Department produced the bonds and helped in designing the bond fixtures. W. King and G. Campbell provided much useful advice on bonding procedures.

References

1. King, W. E., G. H. Campbell, W. L. Wien, and S. L. Stoner (1993), *Strength of Al and Al-Mg/Alumina Bonds Prepared Using Ultrahigh Vacuum Diffusion Bonding*, Lawrence Livermore National Laboratory, Livermore, Calif., (UCRL 53868-93), **6**, pp. 19–22.
2. King, W. E., G. H. Campbell, D. L. Haupt, J. H. Kinney, R. A. Riddle, and W. L. Wien (1995), "X-Ray Tomographic Microscopy Investigation of the Ductile Rupture of an Aluminum Foil Bonded Between Sapphire Blocks," *Scripta Metallurgica et Materialia*, Vol. **33** (12), pp. 1941–1946.

Damage Evolution in Fiber Composite Materials

Steve J. DeTeresa, Scott E. Groves, Dennis C. Freeman,
Patrick J. Harwood, Roberto J. Sanchez, and Marvin A. Zocher
*Manufacturing and Materials Engineering Division
Mechanical Engineering*

Edward Zywicz
*New Technologies Engineering Division
Mechanical Engineering*

The evolution of matrix microcracks and their effects on the elastic and viscoelastic properties of laminated fiber composites was investigated. Proposed models satisfactorily predict the degradation in tensile modulus of cross-ply laminates, but simple ply discounting is a viable alternative. Shear moduli reductions are less than predicted by the models and ply discounting is clearly too drastic. Short-term creep measurements before and after microcracking showed that tensile behavior is elastic, but there is time-dependent behavior in shear which is enhanced by microcracking. A new elastic bend test is being developed in an attempt to determine, for the first time, a fracture energy for fiber tensile failure.

Introduction

One of the strengths of fiber-reinforced structural materials is an ability to sustain relatively high levels of damage without catastrophic failure. The heterogeneous and anisotropic microstructure of these materials contribute to microcracking mechanisms which do not significantly reduce static load-bearing capability of properly designed structures. The accumulated damage can, however, have a significant effect on the thermal elastic and viscoelastic response of the material. For stiffness-critical applications such as dimensionally stable support structures and primary aerospace components, the degradation in these properties can have serious impact on performance.

Additionally, in any modeling scheme that seeks to follow the progression of damage and the concomitant redistribution of stresses, there is a need to know the relationship between constitutive properties and state of damage.

A significant body of theoretical work addresses the problem of predicting the effects of matrix microcracking on the elastic response of fiber composites. This type of damage is shown in **Fig. 1** and is generated in laminated structures by both mechanical and thermal loads. The various models

for predicting the *in-situ* elastic properties of a cracked lamina include, but are not limited to, shear-lag,¹⁻³ minimum complimentary strain energy^{4,5} and internal state variable approaches.⁶

Experimental validation has been restricted mostly to the degradation in tensile modulus and Poisson's ratio in coupon specimens. The one study where the effect of matrix cracking on shear modulus was determined used a cantilever beam technique.³ Because of the non-uniform stress state in the cantilever beam, analysis of the experiment is not straightforward. A preferred method to measure shear properties is torsion of a thin-walled tube, which is the only method that yields pure shear.

We have used a cylindrical specimen and test technique developed previously to simultaneously measure the effects of microcracking on both the tensile and shear moduli of laminates.

Recent work funded under one of our TTI CRADA projects has led to the development of a finite element model for a matrix-cracked viscoelastic laminate.⁷ Similar modeling efforts are planned for the plastic-bonded high explosives and organics in our surviving stockpile. To date there have been no studies to determine experimentally the effects of matrix cracking on the viscoelastic response of composites. As part of our effort to

validate material models, we have investigated the magnitude of enhanced creep in both tension and shear using rectangular coupon and tube specimens.

While matrix cracking is the most prevalent form of damage in fiber composites, damage due to fiber direction stresses can also occur. We have studied the onset of damage in collimated and misaligned fibers under tension.

Progress

Elastic Behavior of Matrix-Cracked Laminates

Thin-walled, 2-in. diameter cross-ply tubes of AS4 carbon fiber and S2 glass fiber with an epoxy resin system (Fiberite 949) were produced with the transverse 90° layer from carbon fiber and the longitudinal 0° layer from either carbon or glass. The 90° layer is cracked during tensile loading in the 0° direction, and moduli in tension and in-plane shear are measured at each crack density.

The loads for these tests are applied as shown in **Fig. 1**. Two lamination patterns were used. A 0ⁱ/90^c₃ laminate where i = c (carbon) or g (glass) allowed cracks in the exposed 90° layer to be monitored directly during the tests using a Microvision MV 2100 video system. The 0° layers of glass are more compliant than the carbon and were selected to allow higher crack densities to develop. Strains were monitored using a biaxial extensometer, designed and constructed by Freeman, which measures axial deformation and rotation simultaneously. Surface-mounted strain gages were ineffective once cracks formed underneath them. Laminates having

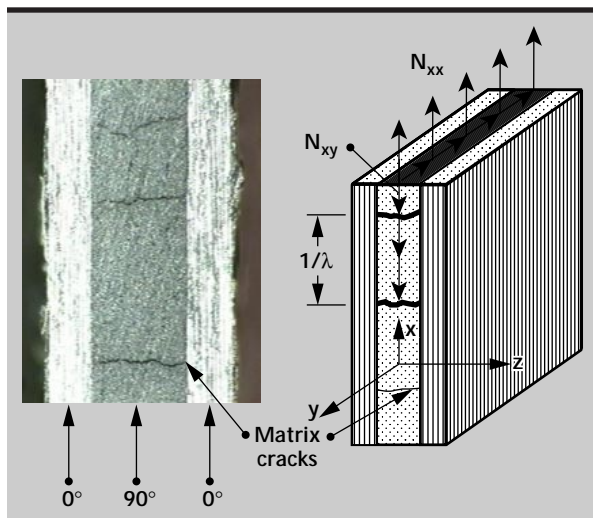


Figure 1. Microcracks in cross-ply laminated fiber composites and coordinates for tensile, N_{xx} , and shear, N_{xy} , loading of damaged materials.

a 0ⁱ/90^c₃/0ⁱ orientation were cracked and measured for moduli, then subsequently sectioned to determine the crack density. Strain gages were used for these specimens. All tests were conducted under tension load and torque control on a MTS biaxial hydraulic test machine.

The evolution of matrix cracks has been modeled using different damage progression schemes. Data collected here were compared to predictions based on a shear lag analysis with a strength criterion² and a strain energy release rate approach.⁵ Each requires a material property (strength or fracture energy) to predict the damage state as a function of the applied stress. Using typical numbers for epoxy composite systems (9 ksi transverse tensile strength and 350 J/m² fracture energy) the fits to data collected for the 0^g/90^c₃ specimens are shown in **Fig. 2**. Reasonable agreement with both models was obtained for the glass/carbon hybrid system, but not the all-carbon system. The same failure parameters were used for each case since the cracked layer in both laminates is the 90^c₃.

The elastic tensile moduli of 0^c/90^c₃ and 0^g/90^c₃ tubes as a function of crack density are compared with shear-lag (Tan-Nuismer) and complimentary energy (Hashin) models in **Fig. 3**. The Hashin model is a lower bound estimate for modulus as evident in the figure. Despite the scattered nature of the test results, it appears that both predictions capture the reduction in tensile modulus with matrix cracking. The data for the glass/carbon hybrid tubes tend toward and below the Hashin prediction. Similar results have been seen for other laminates having exposed 90° layers.⁵

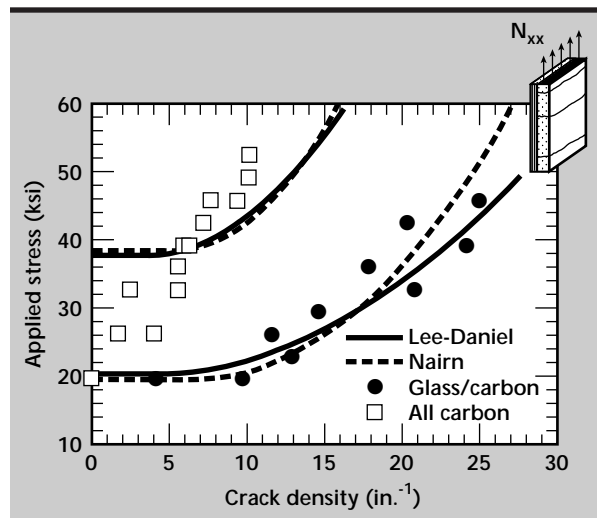


Figure 2. Comparison of microcrack evolution with model predictions for 0ⁱ/90^c₃ tubes.

A possible explanation is that microcracks in these layers form in a more random fashion than those in sandwiched 90° plies, and our observations confirm this. The discrepancy is that the model assumes equal spacing, but the differences are not significant.

In general, the modulus results are in agreement with both model predictions and previous experimental results. Also in the plots shown in **Fig. 3** are the limiting values of modulus reduction obtained by simply “discounting” the properties of the cracked ply. Simple damage progression models use complete discounting (that is, they assign vanishingly small properties) of the damaged ply at the onset of cracking to determine the new stress state. With only moderate levels of damage, which can be seen in **Fig. 2** to be achieved fairly quickly, the tensile modulus approaches this limit. Therefore, the simple ply discount scheme for tensile modulus appears to be a reasonable approximation.

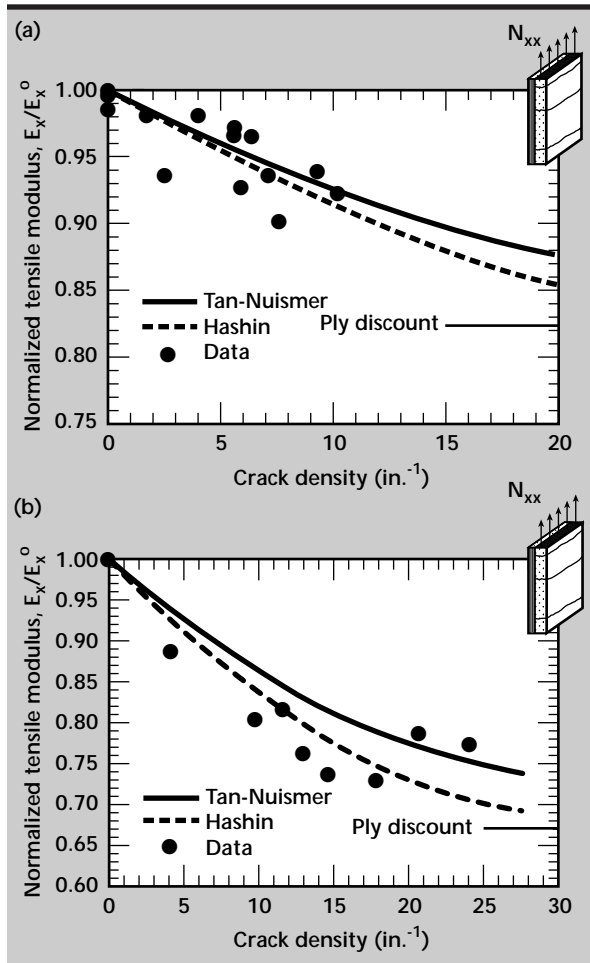


Figure 3. Tensile modulus degradation due to microcracking in (a) $0^\circ/90^\circ/90^\circ$ and (b) $0^\circ/90^\circ/90^\circ$ tubes.

A different result is obtained for the shear moduli of the damaged laminates. **Figure 4** shows the shear modulus reduction for the $0^\circ/90^\circ/90^\circ$ tubes. Similar results were obtained for the other laminates. These are first time results for the effect of matrix cracking on the shear modulus measured in a pure shear mode. In all cases the predicted loss in shear stiffness is greater than measured. Moreover, the ply discount of shear modulus is a gross overestimate of the actual modulus reduction, despite the fact that some high crack densities were generated. In this case it is clear that a damage relationship is needed to adequately model the shear modulus reduction.

Viscoelastic Behavior of Matrix-Cracked Laminates

Several attempts were made to determine the short-term creep response of $0/90_2/0$ laminates in tension and at various temperatures. Despite having near-saturation crack densities exceeding 50/in., no significant difference between the creep of pristine and damaged samples could be found. This loading is fiber-dominated and creep is extremely limited even at temperatures approaching the glass transition temperature of the matrix. We concluded that fiber-dominated behavior is essentially elastic even after significant damage has been accumulated.

Under longitudinal shear, there is significant creep even at room temperature. Because these tests were conducted on the thin-walled tubes in a servo-hydraulic machine under torque control, we were limited to approximately one hour test periods. At longer times, machine drift from a constant torque became a problem.

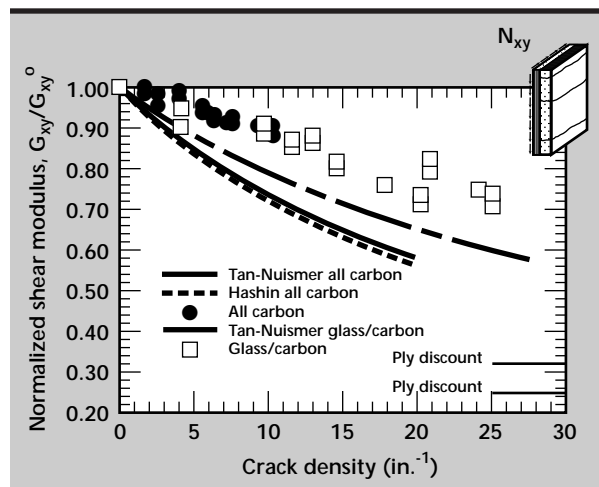


Figure 4. Shear modulus degradation due to microcracking in $0^\circ/90^\circ/90^\circ$ tubes.

An example of the creep curves obtained for a single $0^{\circ}/90^{\circ}_3/0^{\circ}$ tube before and after generating nearly 50 cracks/in. is shown in **Fig. 5**. In addition to the obvious increase in the elastic component of the compliance, there is also a significant increase in the creep rate in the damaged tube. Qualitatively similar results were obtained for the $0^{\circ}/90^{\circ}_3/0^{\circ}$ tubes, but the magnitude of the creep rate increase was much less. This is undoubtedly due to the lower crack densities achieved in these tubes. We are currently analyzing these results using the viscoelastic model developed earlier.⁷

Fiber Direction Damage Modes

During the course of study of the viscoelastic response of $0/90_2/0$ laminates, we discovered that a processing defect in thermoplastic matrix materials severely limited the tensile strength (and, therefore, the attainable crack density) of these composites. The materials are processed above their melt temperatures to achieve adequate consolidation. During cool-down, the difference in thermal expansion between the fiber and tooling can put the fibers in compression. Any fiber compression above the melt temperature cannot be sustained by the composite because the matrix, which supports the fiber against buckling, is a viscoelastic liquid.

The transfer of load into the composite is via a shear lag mechanism, which quickly dissipates through the thickness of the composite. The result is an in-plane microbuckling which occurs periodically near the surface of the specimen. An example of these microbuckles is shown in **Fig. 6**, where the severe fiber misalignment is evident.

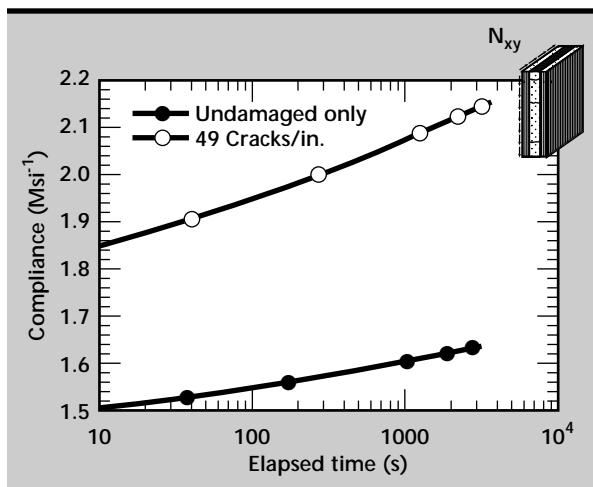


Figure 5. Effect of microcracking on short-term shear creep response of $0^{\circ}/90^{\circ}_3/0^{\circ}$ tubes.

Tensile tests were performed on $0/90_2/0$ specimens having microbuckles in the 0° plies. Failure occurred at about half the expected tensile strength. The failure mode was changed from the normal longitudinal splitting observed for defect-free materials to a predominantly transverse failure surface. Examination of specimens loaded just below ultimate stress levels, such as that shown in **Fig. 6**, revealed that the tensile cracking was initiated at the region of highest misalignment in the microbuckles. Furthermore, the reduction in tensile strength was found to be roughly equivalent to the width of the microbuckle defect at the failure plane. This last observation is consistent with the notch insensitivity of the tough thermoplastic composites.

Our first attempts to generate stable fiber tensile fracture in aligned composites were with hybrid composites of two types of carbon fibers. The fibers were identical except for a nearly 2:1 disparity in tensile strength. It was thought that the failure of the weaker fiber layer would be stabilized by surrounding plies of the high-strength material. However, in all tests, the failure of the weak plies was sudden and complete. Release of the stored elastic strain energy at failure resulted in total delamination between the plies.

To reduce the amount of energy available to propagate cracks once fibers fail, we devised an elastic bend test using thin strips of unidirectional composite. Early results are encouraging in that

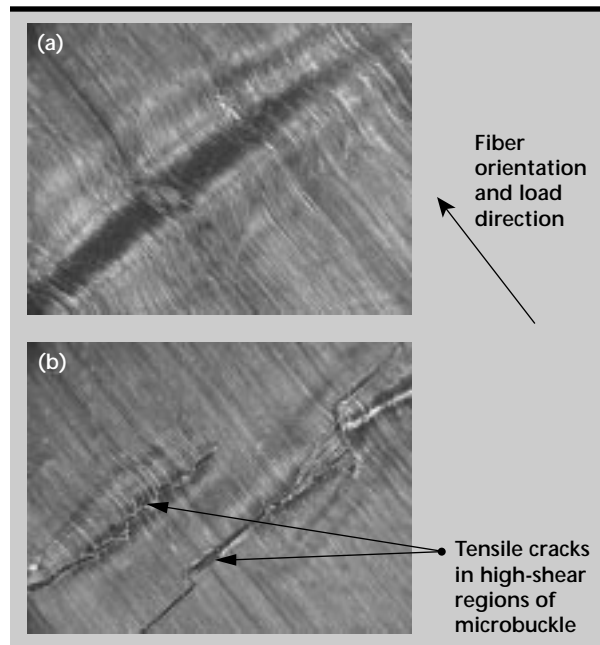


Figure 6. In-plane microbuckle defects (a) and localized tensile fracture (b) in thermoplastic $0^{\circ}/90^{\circ}_2/0^{\circ}$ tubes.

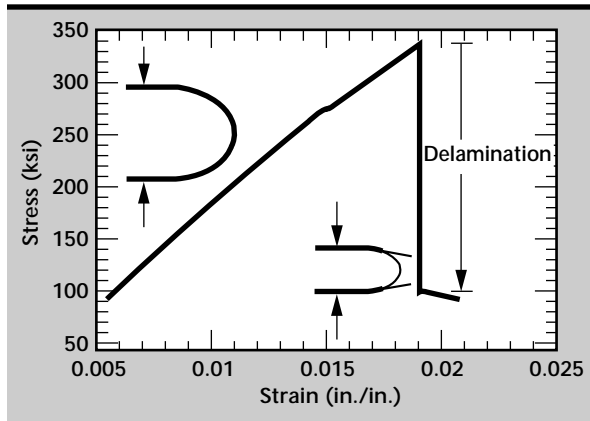


Figure 7. Mechanical response of a thin unidirectional carbon fiber/epoxy strip in the "U-bend" test.


fiber failure results in a degree of delamination which can be measured and therefore potentially analyzed to calculate a fiber fracture energy. Typical results for these "U-bend" tests are shown in Fig. 7. Data are being compared to analysis using a new composite delamination element developed for the NIKE and DYNA structural codes.

Future Work

The viscoelastic response of damaged composites will be compared with results obtained using the finite element model for matrix-cracked viscoelastic laminates. Further developments in modeling the time-dependent response of other composite systems, such as high explosives, in a pristine and damaged state are

needed. The new bend test will be used in conjunction with numerical analysis to determine if a fiber fracture energy can finally be determined.

References

1. Nuismer, R. J., and S. C. Tan (1988), "Constitutive Relations of a Cracked Composite Lamina," *J. Comp. Mater.*, **22**, pp. 306-321.
2. Lee, J.-W., and I. M. Daniel (1990), "Progressive Transverse Cracking of Crossply Laminates," *J. Comp. Mater.*, pp. 1225-1243.
3. Tsai, C.-L., and I. M. Daniel (1991), "The Behavior of Cracked Cross-Ply Composite Laminates Under Simple Shear Loading," *Comp. Eng.*, **1**(1), pp. 3-11.
4. Hashin, Z. (1985), "Analysis of Cracked Laminates: A Variational Approach," *Mech. Mater.*, **4**, pp. 121-136.
5. Nairn, J. A. (1989), "The Strain Energy Release Rate of Composite Microcracking: A Variational Approach," *J. Comp. Mater.*, **23**, pp. 1106-1129.
6. Lee, J.-W., D. H. Allen, and C. E. Harris (1989), "Internal State Variable Approach for Predicting Stiffness Reductions in Fibrous Laminated Composites with Matrix Cracks," *J. Comp. Mater.*, **23**, pp. 1273-1291.
7. Zocher, M. A., D. H. Allen, and S. E. Groves (1996), "Stress Analysis of a Matrix-Cracked Viscoelastic Laminate," *Int. J. Solid. Struct.* (in press). 

F

Flashlamp Envelope Optical Properties and Failure Analysis

Mark A. Havstad
Laser Science Engineering Division
Mechanical Engineering

We have measured the high-temperature transmittance of cerium-doped quartz. Measurements were made in the ultraviolet and visible spectral ranges (0.25 to 0.7 μm) for sample temperatures from 26 to 1000 $^{\circ}\text{C}$. Cerium-doped quartz is of interest because it is the envelope material for the 10,000 flashlamps planned for the National Ignition Facility (NIF) at Lawrence Livermore National Laboratory (LLNL). Our measurements of the increase in absorption of the doped quartz quantify the decrease in performance of the lamps as they heat during each firing cycle. They also make it possible to calculate the transient thermal stress in an envelope due to temperature-dependent absorption through the material thickness. Our data has been used to show that it is unlikely that temperature-dependent absorption plays a role in the catastrophic flashlamp failure mode sometimes observed early in the lifetime of a lamp.

Introduction

The great majority of optical elements and materials operate below 100 $^{\circ}\text{C}$. In many applications excursions in excess of a few degrees from room temperature are avoided. Similarly, the sophisticated and precise instruments evolved by the optics industry are rarely capable of treating samples at elevated temperatures. However, the transmittance of the glass envelopes of flashlamps, commonly used to provide the optical pumping in a wide range of laser systems, plays an important part in the system performance, lifetime, and operating conditions for material temperature ranging from ambient to 800 $^{\circ}\text{C}$.

The cerium-doped quartz envelopes of the flashlamps planned for LLNL's NIF are a key component because they transmit both pump band energy (0.4 to 1.0 μm) for the laser amplifiers and thermal energy (beyond 1.0 μm) and UV energy (below .4 μm). The thermal energy heats the laser slab and causes a wait of several hours before the slab is sufficiently cool and uniform in temperature to fire again (adequate beam quality and no risk of fracture of the laser slab due to thermal stress are concerns). The UV energy damages materials with each firing and reduces the lifetime of components.

Not only is flashlamp transmission important to NIF operation, absorption of flashlamp radiation in its own envelope is also a concern because heating

causes more absorption, reduced lamp output, and transient thermal stress. During the early portion of the 350- μs firing period the room-temperature and low-temperature transmittance of the envelopes is operative, but by the final portions the transmittance at 800 $^{\circ}\text{C}$ causes heating on the inner skin of the envelope and constitutes a positive feedback loop where absorption causes heating, which causes more absorption. Since the absorption is not uniformly distributed over the thickness of the envelope, one expects a resultant transient thermal stress that could cause lamp failure (explosion of the envelope).

In this report we present our measurement methods and the temperature-dependence of the transmittance of cerium-doped quartz from 0.25 to 0.75 μm for temperatures from 26 to 1000 $^{\circ}\text{C}$. Last year we presented visible and near infrared transmittance measurements for this material, but with a very coarse spectral resolution and only at 400, 600, 800 and 1000 $^{\circ}\text{C}$. This year we revised our optical system to reach the UV range and to obtain much finer resolution, both in temperature and wavelength. Our measurements of last year indicated that there was little temperature-dependent absorption from the far end of the visible to 1 μm , so we have limited ourselves to 0.25 to 0.75 μm in the present study.

Progress

The optical system (shown in **Fig. 1**) was designed to be used over a broad spectral range, 0.2 to 9 μm . The carbon filament lamp (power usage 24 A at 12 V DC), imaged along the vacuum furnace axis by the spherical mirror on a kinematic base is useful in the visible and IR. The arc lamp (200-W mercury/xenon bulb), imaged by a UV-grade fused-silica lens, provides UV, visible and near IR output. For visible and UV measurements the carbon lamp is off and the spherical mirror is removed from the kinematic base. This arrangement allows both light sources to be imaged down the furnace axis and, once aligned, to be fixed in position. Apertures along this optic axis limit the beam to a diameter of 0.6 mm.

The furnace includes a 102-mm long by 64-mm diameter heating element (0.64-mm thick carbon composite) which dissipates 600 W of DC power at 21 A to give sample temperatures of 1000 $^{\circ}\text{C}$. Samples are held in graphite rings that are supported by four alumina rods that span the axial length of the hot zone and are themselves supported by the niobium thermal shields at either end of the furnace. A clear aperture of 12.7 mm diameter is bored through the thermal shields for the transmitted beam, but larger beams could be accommodated; the graphite rings holding the sample allow a clear aperture through the sample as large as 40 mm.

Five layers of thermal shielding are used at the furnace ends and around the furnace circumference. These last shields isolate the hot zone from a water cooled jacket that is fitted between the shields and the vacuum vessel walls.

The furnace is pumped by a 60 l/s turbomolecular pump backed by a mechanical roughing pump. The windows for optic access are calcium fluoride disks mounted in conflat vacuum flanges by a commercially proprietary silver brazing process. The window on the entrance side is mounted in a 33.8-mm O.D. flange and has a clear aperture of 11.8 mm and, on the exit side, a 69.8-mm flange with a clear aperture of 32.4 mm.

The optical system uses two beam paths: a sample path where the beam passes through the furnace and the sample, and a reference path where the beam is diverted by a turning mirror and routed to the detector by a path which remains at essentially room temperature for the duration of the measurements. The reference path (~210 cm long) is equal in length to the sample path (to within about 1 cm). The two turning mirrors in each path were fabricated on the same coating run. The focusing lens, filter and detectors common to the two beam paths are relatively isolated from the furnace thermal emission.

During initial optical alignment through the furnace, the output of the two light sources is imaged on the far wall of the laboratory so that the

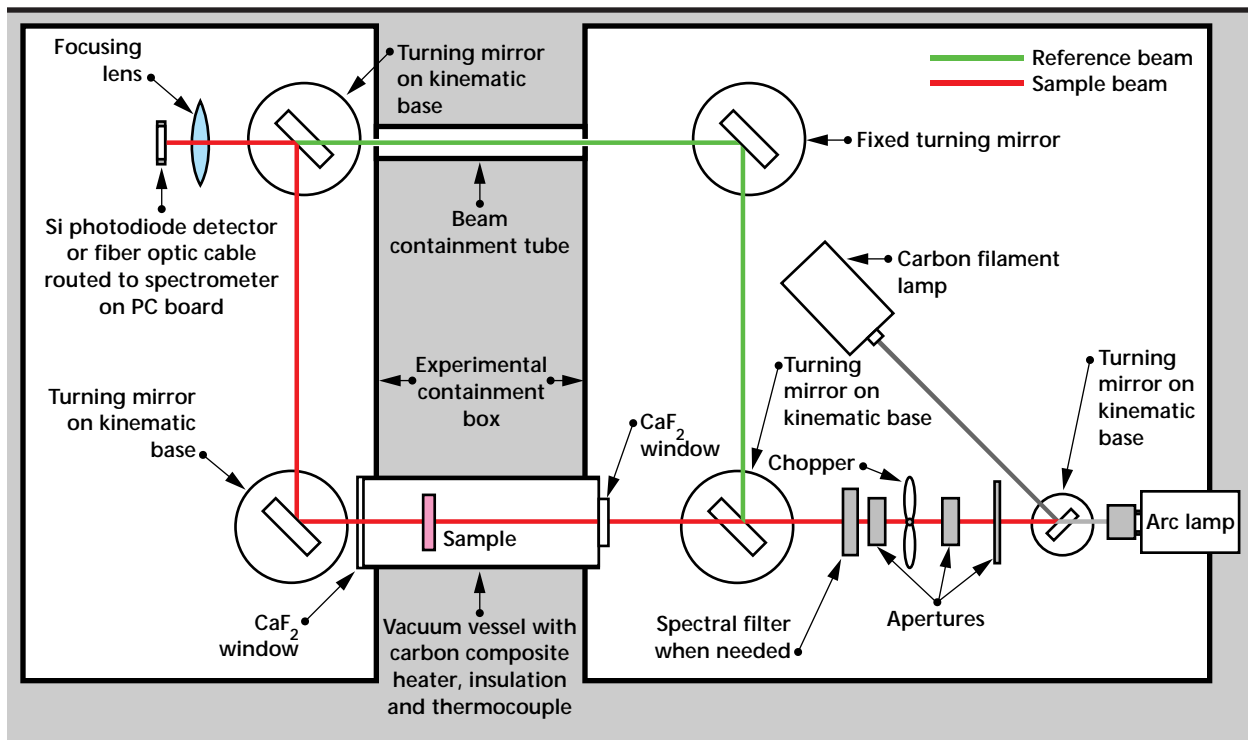


Figure 1. Schematic of optical system.

light incident on the sample is nearly collimated. Since all the turning mirrors are planar, the thermal emission from the furnace is not imaged at the detector and its intensity declines as the square of the distance from the furnace to the focusing lens.

The CaF₂ focusing lens images either of the light sources on the detection optics. For spectrally coarse measurements a bandpass filter is placed between the the lens and a silicon photodiode or an InSb/HgCdTe sandwich detector. For this system, the chopper, a lock-in amplifier and a diode pre-amplifier make up a phase-sensitive detection system. For more spectrally-resolved measurements (0.25 to 0.7 μm) the transmitted beam is imaged into an optical fiber. The fiber extends to a commercially supplied computer board. At the board back plane are a lens, a miniature grating and a 1024-element CCD detector array. The spectral calibration (pixel number to wavelength) is provided with the board and can be checked with any light source with sharp spectral lines.

The detector response for the sample and beam paths (minus the system dark signal) can be represented by:

$$V_{sam} - V_{dar} = B_s \cdot \tau_{W1} \cdot \tau_{sam} \cdot \tau_{W2} \cdot \rho_{T1} \cdot \rho_{T2} \cdot \tau_L \cdot \tau_f \cdot R_D$$

$$V_{ref} - V_{dar} = B_{s'} \cdot \rho_{T3} \cdot \rho_{T4} \cdot \tau_{L'} \cdot \tau_{f'} \cdot R_{D'}$$

where ρ is the turning mirror reflectivity, τ is transmittance, R_D is detector responsivity and B_s is lamp output through the chopper and apertures. Subscripts L, f, T1, T2, T3 and T4 refer to the focusing lens, bandpass filter and turning mirrors. Subscripts W1 and W2 refer to the entrance and exit windows on the furnace. The use of a prime symbol on some of the subscripts indicates a second order deviation between the primed and unprimed values. For example, the transmittance of the focusing lens is nominally the same for either beam path, but small differences in beam size or incident angle for example, result in slight deviations.

At any given wavelength and sample temperature, the ratio of transmittance at temperature to the transmittance at room temperature is computed from the above two relations:

$$\frac{\tau(temp)}{\tau(amb)} = \frac{\left(\frac{B_s \cdot \tau_{W1} \cdot \tau_{W2} \cdot \rho_{T1} \cdot \rho_{T2} \cdot \tau_L \cdot \tau_f \cdot R_D}{B_s \cdot \rho_{T3} \cdot \rho_{T4} \cdot \tau_{L'} \cdot \tau_{f'} \cdot R_{D'}} \right)_{temp}}{\left(\frac{B_s \cdot \tau_{W1} \cdot \tau_{sam} \cdot \tau_{W2} \cdot \rho_{T1} \cdot \rho_{T2} \cdot \tau_L \cdot \tau_f \cdot R_D}{B_s \cdot \rho_{T3} \cdot \rho_{T4} \cdot \tau_{L'} \cdot \tau_{f'} \cdot R_{D'}} \right)_{amb}}$$

Thus the apparatus is used to make a relative transmittance measurement, τ_{hot}/τ_{amb}. A Carey 5 spectrophotometer, was used to make a precision absolute transmittance measurement at room temperature.

The temperature-dependent transmittance of a cerium-doped quartz sample provided from LLNL's NIF development work is shown in Fig. 2. Absorption in the UV and short wavelength portion of the visible increases with temperature. The short wavelength cut-off in transmission shifts to longer wavelengths steadily at a rate of approximately 3 nm per 100 °C.

The increase in absorption in the UV is desirable from the viewpoint of reducing damaging UV passed from the lamp to the remainder of the laser system, and is probably inconsequential to lamp failure mechanisms. It would take a much larger effect with temperature to account for lamp heating leading to explosion. The shift in the absorption edge to longer wavelengths is unwanted because it reduces the pump band output of the flashlamp, but the shift noted here is modest and most of it confined to wavelengths less than those designated as pump band, 0.4 to 1.0 μm.

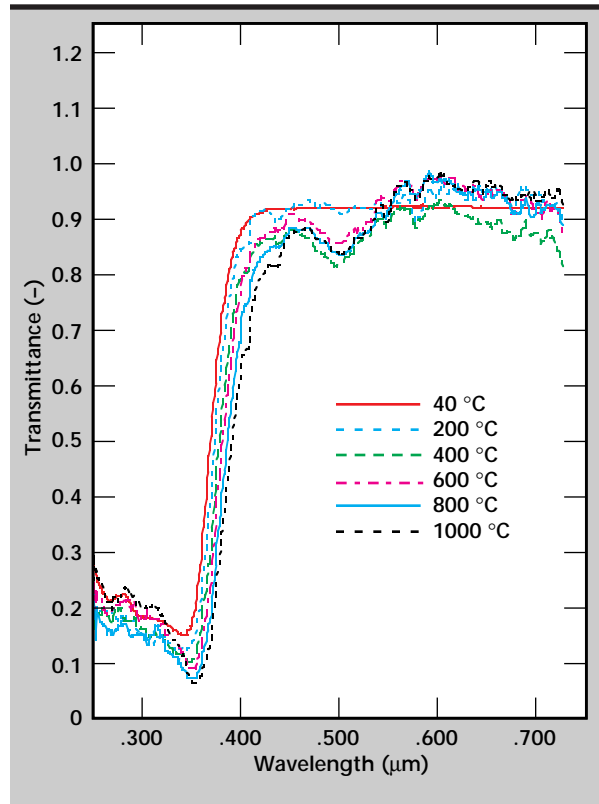


Figure 2. Transmittance of cerium-doped quartz in the ultraviolet and visible regions.

A second unwanted but also modest effect is the absorption at .500 μm. This feature as well as the decline in transmission at .400 μm can be observed in last year's work (with coarse spectral resolution), but here they are well quantified. The data shown indicates that there are no absorption phenomena of significance beyond .550 μm (as was indicated in previous work also), but quantitatively the indication of higher transmittance at elevated temperature than at ambient is probably incorrect.

The optical constants of cerium-doped quartz, which determine the material transmittance, can be formulated several ways; for example, by the index of refraction and the extinction coefficient, k, or the index and the absorption coefficient, $\mu = 4\pi k/\lambda$.

Computation of the absorption coefficient (which contributes to the transient thermal stress in the envelope of each flash) from a single transmittance measurement requires an assumption concerning the relationship between the two optical constants. Here we assume that in the short wavelength portion of the spectrum, up to .36 μm, a collection of 8 Lorentz oscillators adequately characterizes the relationship between the optical constants:

$$\epsilon^c = (\epsilon^a)_s + \sum_{j=1}^n \frac{(v_j)^2 \cdot \Delta\epsilon_j}{(v_j)^2 - v^2 + z \cdot v \cdot \gamma_j}$$

The complex permittivity is ϵ^c (yet another pair constituting the optical constants), v is the

Table 1. Oscillator parameters calculated from least squares fit.

	Temp. (°C)					
	26	200	400	600	800	1000
Oscillator number	Mode strength (dimensionless)					
1	0.138	0.467	0.2	0.116	0.182	0.394
2	0.618	0.796	1.616	2.107	2.514	3.404
3	0.7	0.8	0.8	0.7	0.8	0.7
4	0.3	0.4	0.4	0.3	0.4	0.3
5	8	8.7	8.7	8	9	7
6	1.5	1.9	1.9	1.8	2	1.9
7	0.3	0.4	0.4	0.3	0.5	0.3
8	7.02	7.25	7.25	7.02	7.5	6
	Linewidth (damping)÷oscillator frequency (dimensionless)					
1	0.027	0.071	0.05	0.039	0.031	0.055
2	0.043	0.054	0.064	0.058	0.063	0.065
3	0.2	0.2	0.2	0.2	0.2	0.2
4	0.15	0.15	0.15	0.15	0.15	0.15
5	0.3	0.3	0.3	0.3	0.3	0.3
6	0.12	0.12	0.12	0.12	0.12	0.12
7	0.04	0.04	0.04	0.04	0.04	0.04
8	0.319	0.319	0.319	0.319	0.319	0.319
	Oscillator mode (location of resonance) v (nm)					
1	338	338	338	338	338	338
2	347	349	350	351	353	355
3	280	280	280	280	280	280
4	313	313	313	313	313	313
5	335	335	335	335	335	335
6	263	263	263	263	263	263
7	252	252	252	252	252	252
8	300	300	300	300	300	300

wavenumber, $\Delta\epsilon_j$ is the oscillator strength (or plasma frequency), ν_j is the oscillator resonant frequency and γ_j is the damping constant. The static dielectric constant is $(\epsilon^c)_s$. All quantities except the wavenumber are functions of temperature.

This equation satisfies the Kramers-Kronig relations, and thus provides a physically consistent relationship between the two optical constants.¹ The choice of modes (oscillator resonant frequencies) is somewhat arbitrary, particularly in the shortest wavelength ranges, but the fit as shown here gives a close match to the data and yields a real index of refraction that is consistent with previously published data for quartz at room temperature.² For the 0.25- to 0.36- μm range the oscillator parameters obtained from least squares fitting of the measurements are given in **Table 1**.

For wavelengths beyond 0.36 μm the absorption edge is well fit by the ‘‘Urbach rule’’³:

$$\mu(\nu, T) = \mu_o \cdot \exp[-b \cdot (E_o - E(\nu))]$$

$$\tau(\nu, T) = (1 - \rho)^2 \cdot \exp(-\mu(\nu, T) \cdot t) \quad .$$

The absorption coefficient at ambient is μ_o , photon energy is $E=h\nu$, E_o is the bandgap, and b is the steepness parameter. The part thickness is t and ρ is the reflectivity (actually also a function of wavenumber and temperature, but in the absorption edge region and to longer wavelengths within the visible, the dependence of ρ on either ν or T is insignificant). Various explanations for this dependence of the absorption edge on wavelength have

been given, including thermal fluctuation of the bandgap and electric fields arising from defects, phonons, and impurities.^{4,5}

The transmittance data for ambient has been fit to the relations above (for wavelengths from 0.36 to 0.45 μm) with four parameters (μ_o , E_o , b , and ρ) varied until the sum of the squared error was minimized. The data at elevated temperature was fit similarly, but with ρ fixed and just the other three variables minimized. The results of these fits are given in **Table 2**.

Of the three quantities (μ_o , E_o , and ρ_o) varied to obtain each elevated temperature fit, μ_o is approximately constant and the other two are well fit to linear functions (**Fig. 3**). The shift of E_o with temperature, a shift of the Urbach tail to longer

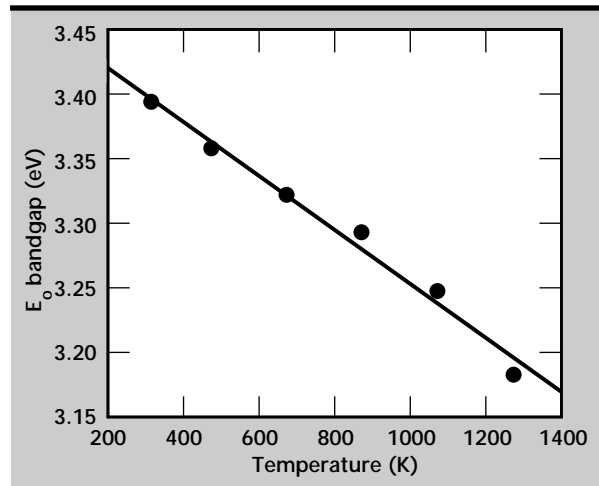


Figure 3. Shift in bandgap energy fit to linear function.

Table 2. Transmittance data.

Temperature (°C)	μ_o (1/cm)	b (1/eV)	E_o (eV)
26	307.9	8.508	3.394
200	308.6	8.131	3.358
400	319	6.767	3.322
600	312.4	7.088	3.293
800	302.4	6.323	3.248
1000	260.6	5.801	3.183
Average	301.8	linear	linear

Reflectance = 0.039

$y = mx + b$		
	m	b
E_o	-2.08×10^{-4}	3.4619
b	-2.73×10^{-3}	9.234

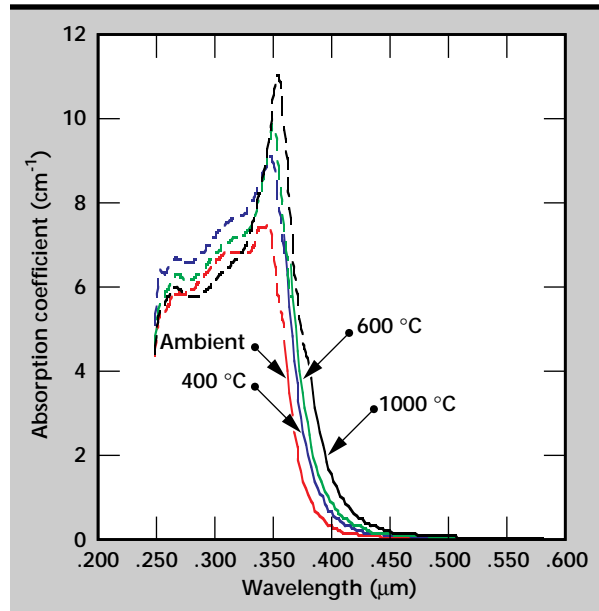



Figure 4. Absorption coefficient of cerium-doped quartz.

wavelengths, is common in insulators and semiconductors. As temperature increases the short and long wavelength limits of transparency tend to shift inwards, shrinking the region of transmission.

The oscillator and Urbach models allow a compact specification of the transmission data or the absorption coefficient for use in computer modelling of radiant transport and transient thermal stress in the flashlamp envelope. The absorption coefficient computed from the parameters in **Tables 1** and **2** is plotted in **Fig. 4** for four temperatures. The models do not attempt to match the absorption noted in **Fig. 2** at 0.50 μm ; a more complex model for the absorption would have to be developed to match that region as well.

This data has been provided to computer models which have estimated the spectral and temperature-dependent absorption through the thickness of a simulated flashlamp envelope. Thermal stress calculations were then used to estimate transient thermal stress in the cerium-doped quartz.⁶

References

1. Thomas, M. E. (1991), "Temperature-Dependence of the Complex Index of Refraction," *Handbook of Optical constants of Solids II*, Academic Press, New York, p. 177.
2. Myers, V. H., A. Ono, and D. P. DeWitt (1986), "A Method for Measuring Optical Properties of Semitransparent Materials at High Temperatures," *AIAA Journal* **24**, pp. 321–326.
3. Lynch, D. W. (1985), "Interband Absorption - Mechanisms and Interpretation," *Handbook of Optical Constants of Solids*, Academic Press, New York, p. 189.
4. Skettrup, T. (1978), "Urbach's Rule Derived from Thermal Fluctuations in the Bandgap Energy," *Phys. Rev. B* **18** p. 2622.
5. Dow, J. P., and D. Redfield (1972), "Toward a Unified Theory of Urbach's Rule and Exponential Absorption Edges," *Phys. Rev. B* **5**, p. 594.
6. Maltby, J., V. C. Garcia, and B. T. Kornblum (1996), "Radiation-Induced Thermal Stresses in High-Power Flashlamps," *Engineering Research, Development and Technology*, Lawrence Livermore National Laboratory, Livermore, Calif., UCRL-53868-96. 

Synthesis and Processing of Nanocrystalline Hydroxyapatite

T. G. Nieh
*Materials Science and Technology
Chemistry*

Donald R. Lesuer
*Engineering Sciences
Mechanical Engineering*

We have developed a technique to construct bulk hydroxyapatite (HA) with different cellular structures. The technique involves the initial synthesis of nanocrystalline HA powder from an aqueous solution using water-soluble compounds, followed by spray-drying into agglomerated granule. Depending upon the processing parameters, the morphology of the spray-dried granules can be varied. The granules were further cold-pressed and sintered into bulks at elevated temperatures. Since the starting HA powders were extremely fine, a relatively low activation energy (21.3 kJ/mol) for sintering was obtained. From the sintering study, both porous and dense structures were produced by varying powder morphology and sintering parameters.

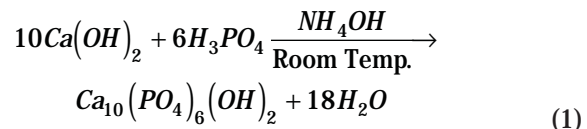
Introduction

Calcium phosphate apatite (CPA) is one of the most viable implantable materials because of its biocompatibility. The major subphase of the bone mineral consists of submicroscopic crystals of an apatite of calcium and phosphate, resembling HA in its crystal structure $[\text{Ca}_{10}(\text{PO}_4)_6(\text{OH})_2]$. The HA is nanocrystalline with grains ranging in size from 10 to 50 nm. These nano-sized grains are hierarchically assembled into connective hard tissue, that is, bone-skeleton.

Currently, there are three types of bone grafting: autograft, allograft, and synthetic (that is, coralline blocks). Recent research has been performed to develop composite materials such as HA/bioglass® ceramic composites with ZrO_2 , Al_2O_3 and SiO_2 , and HA/bioglass® polymer composites.¹ However, cellular structures with macro- ($> 100 \mu\text{m}$) and micro-interconnected pores made directly from HA and with sufficient fracture strength have not been successfully produced. This research is aimed at constructing various HA cellular solids (bone-like) from nanocrystals.

Progress

The chemical precipitation method used to synthesize HA particles is described by the following chemical reaction:



The precipitated HA reveals a needle-shaped morphology (~10 to 20 nm in width and 60 to 90 nm in length), similar to that of the apatite particles existing in natural bones. These needle-shaped nanocrystalline particles were further suspended and sprayed, resulting in large-sized powders with different shapes.

The sprayed powders were cold-pressed into green bodies (density = $1.42 \pm 0.15 \text{ g/cm}^3$, approximately 44% of the theoretical density) at a uniaxial pressure of 187 MPa. The green bodies were sintered for 4 h in air at temperatures varying from 700 to 1300 °C. Experimental results are listed in **Table 1**. As indicated, the density value increases with sintering temperature and reaches a nearly fully dense value (99%) at the sintering temperature of 1300 °C. The micro-hardness values, H_v , ranging from 208 to 483 MPa, were also found to increase with sintering temperature. The grain structure of the 99%-dense sample is shown in **Fig. 1**, which revealed equilibrated, hexagonal-shaped grains with sharp apexes with a mean grain size of about 4 μm . X-ray analysis indicates that the sample also contains a slight amount of whitlockite (TCP), which

is somewhat expected, since apatite is essentially a line compound and technically difficult to obtain in pure form.

The density of sintered samples as a function of temperature is plotted in **Fig. 2**. Within the temperature range of the present study, density increases monotonically with sintering temperature. Data from the literature^{2,3} are also included in **Fig. 2** for comparison. Our density values are noted to be higher than those reported previously.^{2,3} This is because the starting HA powders used in the present study are ultrafine (nanocrystalline). Therefore, there exists an exceedingly large amount of surface energy acting as an additional thermodynamic driving force for sintering. In addition, enhanced diffusion processes (that is, short-circuit diffusion) are expected to operate, as discussed later. Both factors tend to accelerate the sintering process.

The shrinkage of a non-transforming solid during sintering, assuming a non-isothermal process, can be described by **Eq. 2**⁴

$$S\% = k \exp(-Q / RT)t^{1+n} \quad (2)$$

where t is the sintering time, Q is the activation energy, T is the absolute temperature, R ($= 8.314 \text{ J/mol}$) is the gas constant, k is a constant, and n is a constant which is about 0.3 to 0.4 for oxide ceramics. From **Eq. 2**, the activation energy for sintering can be computed. It is calculated to be 21.3 kJ/mol (5 kcal/mol), which is significantly lower than those reported previously ($\sim 200 \text{ kJ/mol}$). The relatively low activation energy agreed with the early suggestion that short-circuit diffusion processes (for example, surface and interface diffusion) dominate during the sintering of nanocrystalline HA.

Recent clinical tests indicated that the optimum pore size for an implant with a cellular structure ought to be greater than $100 \mu\text{m}$.^{5,6} At this size, soft body tissues are able to exhibit a good ingrowth while the implant still retains its mechanical integrity. In the present research, several efforts were made to fabricate HA with a cellular structure.

Table 1. Physical properties of sintered HA at various temperatures.

Temperature (°C)	Relative density (ρ %)	Shrinkage (S%)	Micro-hardness (Hv)
1300	99	55	483
1200	88	50	—
1180	84.5	48	—
1100	84	47.6	303
1000	71	38	263
900	64	31	208
700	44	0	—
Green body	44	—	—

Figure 1. The grain structure of the 99%-dense sample, revealing equilibrated, hexagonal-shaped grains with sharp apexes, with a mean grain size of about $4 \mu\text{m}$.



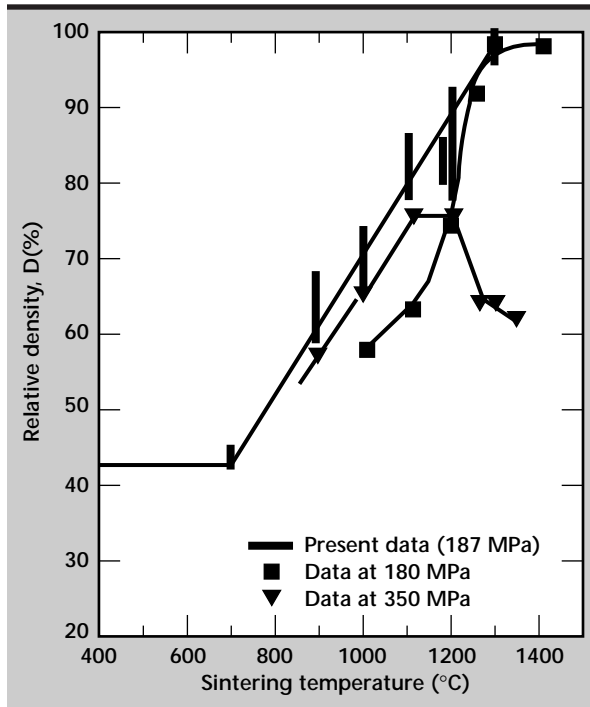


Figure 2. Relative density of sintered HA as a function of temperature.

Based upon the sintering results, experiments were carried out by adding polymer beads with a diameter of approximately 100 μm to HA in the green state. The polymer beads were subsequently pyrolyzed during high-temperature sintering to stimulate the formation of interconnected macro-pores in HA skeleton. The sintering temperatures of 1000 and 1100 $^{\circ}\text{C}$ were selected.

Figure 3 is the SEM surface morphology of the composite sample (HA plus polymer beads) sintered at 1100 $^{\circ}\text{C}$ for 4 h. The sample has a density of 55% with a mean pore size of about 20 μm , and the pore distribution is relatively uniform. SEM stereo projection indicates that the pores are interconnected. The 3-D interconnectivity of these pores was further confirmed with x-tomographic microscopy.

Future Work

This research will not be continued in FY-97.

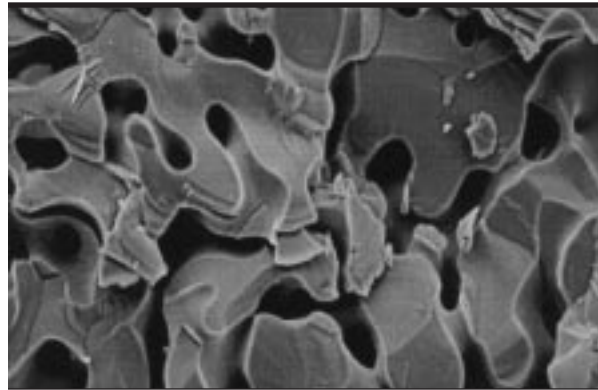


Figure 3. SEM surface morphology of the composite (HA plus polymer beads) sintered at 1100 $^{\circ}\text{C}$ for 4 h.

References

1. Wilson, J., L. L. Hench, and D. Greenspan (1995), *Bioceramics, Volume 8*, Pergamon/Elsevier Science Ltd., Oxford.
2. Goto, T., N. Wakamatsu, H. Kamemizu, M. Iijima, Y. Doi, and Y. Moriwaki (1991), "Sintering Mechanism of Hydroxyapatite by Addition of Lithium Phosphate," *J. Mater. Sci.—Medicine*, **2**, pp. 149–152.
3. Wang, P. E., and T. K. Chaki (1993), "Sintering Behavior and Mechanical Properties of Hydroxyapatite and Dicalcium Phosphate," *J. Mater. Sci.—Medicine*, **4**, pp. 150–158.
4. Kingery, W. D., H. K. Bowen, and D. R. Uhlmann (1976), *Introduction to Ceramics*, John Wiley & Sons, Inc., New York, N.Y.
5. Klawitter, J. J., and S. F. Hulbert (1971), "Application of Porous Ceramics for the Attachment of Load Bearing Orthopedic Application," *J. Biomed. Mater. Res. Symp.*, **2**, pp. 161–169.
6. Hench, L., and J. Wilson (1993), *An Introduction to Bioceramics*, World Scientific Publishing Co. Ltd., Singapore.

Room Temperature Creep Compliance of Bulk Kel-F

Marvin A. Zocher, Steve J. DeTeresa, and Scott E. Groves
Manufacturing and Materials Engineering Division
Mechanical Engineering

Experiments have been conducted to determine the room temperature tensile creep compliance of bulk Kel-F 800. Tests of linearity have been included as well. Specimens were subjected to loads resulting in nominal homogeneous stress states of 138, 310, and 490 kPa. Under all three loading conditions, the material was observed to be linear. The degree of crystallinity in the specimens tested was low. They were essentially amorphous.

Introduction

Kel-F 800 is a copolymer formed from the monomers chlorotrifluoroethylene (CTFE) and vinylidene fluoride (VF). The nominal composition consists of a 3:1 mole ratio of CTFE to VF, with the monomers arranged in random alternation. Kel-F 800 also contains a small amount (< 2 wt%) of perfluorodecanoic acid, which is added as an emulsifier. Originally developed by the M. W. Kellogg Company, it is now manufactured by 3M where it is referred to as FK-800.

In bulk form, the copolymer is a thermoplastic and has a T_g of about 31 °C. Kel-F 800 is used by Lawrence Livermore National Laboratory (LLNL) as the binder for the explosive 1,3,5-triamino-2,4,6-trinitrobenzene (TATB) in the plastic bonded explosive (PBX) LX-17. LX-17 is 92.5% (by weight) TATB and 7.5% Kel-F 800. The Los Alamos National Laboratory (LANL) PBX-9502 is similar to LX-17, consisting of 95% TATB and 5% Kel-F 800.

The thermo-mechanical behavior of Kel-F 800 is not well characterized at the present time. The literature contains data on tensile properties determined from quasi-static testing, and on shear properties determined from dynamic mechanical analysis (DMA).¹⁻⁴ Cady and Caley¹ performed tensile tests on dog-bone specimens cut from molded sheets having a uniform thickness of 0.05 cm. These tests were conducted in an Instron loading machine with cross-head speeds of 0.127, 1.27, and 25.4 cm/min. All tests were conducted at room temperature (RT). Tensile yield was observed to increase linearly with degree of crystallinity (DOC) while ultimate elongation decreased linearly with DOC. Ultimate strength was found to be

largely independent of DOC. The DMA tests were conducted in the forced torsional pendulum mode at 0.2 Hz over a temperature range of -160 to 110 °C.

Grotheer² performed DMA tests in the forced torsional pendulum mode at 1 Hz over a temperature range of -75 to 100 °C. Grotheer's specimens were cut from sheets molded at 80 °C (Cady and Caley did not address the processing of the sheets from which specimens were taken).

Hoffman, Matthews, and Pruneda³ performed DMA and DSC on specimens molded under moderate pressure at 120 °C (the processing temperature for molding LX-17). The DMA was conducted over a temperature range of -100 to 150 °C using five different frequencies.

DMA has been conducted by Herold⁴ as well. Additional data on Kel-F 800 may be found in the LLNL Explosives Handbook⁵ and in a survey, currently under way, by Overturf and LeMay.⁶

The objective of the current program was to add to our understanding of the thermo-mechanical behavior of Kel-F 800, particularly with respect to time-dependent behavior. In keeping with this, experiments have been conducted for the purpose of determining the RT creep compliance of bulk Kel-F 800. Tests of linearity have been included in the experimental program.

Progress

Specimen Fabrication

As alluded to in the previous section, DOC can have a strong influence on the thermo-mechanical response of Kel-F 800. The DOC is in turn

strongly influenced by thermal history. Consequently, it is the opinion of the authors that any data presented on Kel-F 800 that is not accompanied by processing history and an assessment of DOC is of little value.

Kel-F 800 comes from the manufacturer in a form that is similar in appearance to common rock salt, but with a subtle yellowish tint. This raw material was molded into sheets, roughly 28 cm in diameter and 2 mm thick. This was accomplished with heat and pressure. The method used for processing the sheets is as follows:

Step 1. 150 g of Kel-F 800 was heated at 120 °C for 1 h in a crude mold (a hose clamp lined with Kapton film) measuring approximately 10 cm in diameter, with a height of approximately 1.3 cm. After an air cool, the Kel-F was removed from the mold as a loosely consolidated disk, looking similar to a rice cake. Thirty-two such disks were formed, one for each sheet to be processed.

Step 2. Processing of the disk was accomplished in a 667 kN PHI 4-post hydraulic press with platens roughly 61 cm × 76 cm. This platen area was large enough for four sheets to be formed at a time. The processing region of the PHI was fitted with a furnace. Sheets of Kapton were

used to prevent the Kel-F 800 from adhering to the platens.

- The oven was preheated to 120 °C per thermocouple located at the center of the platens.
- Once the temperature was stabilized at 120 °C, the samples were loaded to 106.76 kN (24,000 lb_f) in compression at a loading rate of 53.38 kN (12,000 lb_f)/min. The samples were held at 106.67 kN (24,000 lb_f) for 3 min, then unloaded to about 445 N (100 lb_f) and held at that load for 1 min. The unloading rate was the same as the loading rate, that is, 53.38 kN/min.
- The load/unload cycle described above was repeated three times (**Fig. 1**). The processed sheets were then allowed to air cool.

Uniaxial tension specimens (**Fig. 2**) were cut from these sheets using a “cookie-cutter” type of stamp (MMED Stamp No. 18816) which is based on ASTM D412. Each of the 32 sheets was large enough to provide either five or six tensile specimens (most provided six). Approximately 12 specimens were used to establish test procedures and 20 were used in the current study of RT creep compliance. This leaves several specimens available for follow-on work.

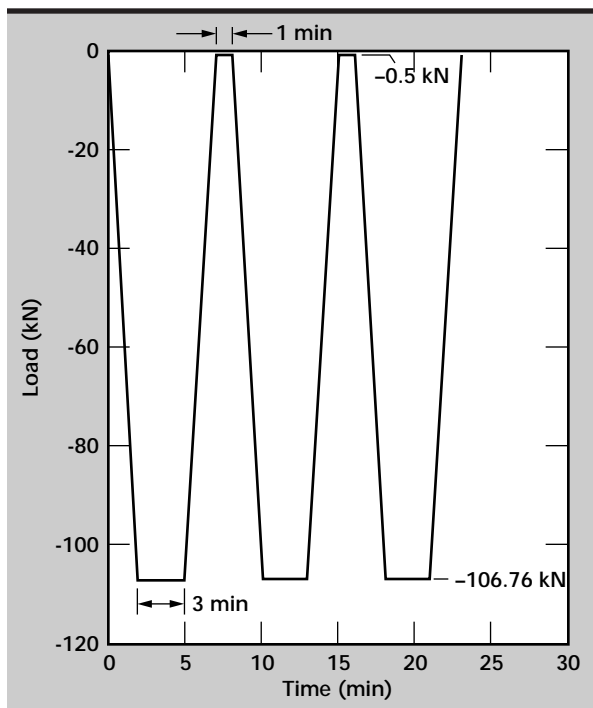


Figure 1. Pressing sequence.

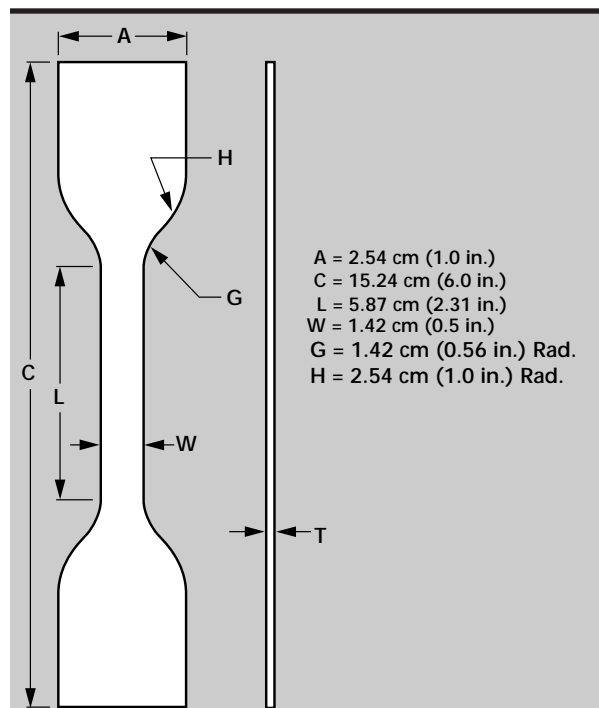


Figure 2. Specimen geometry.

Test Procedures

Both creep and creep-and-recovery tests were conducted at three different load levels. These tests were conducted in a room maintained at 21.5 °C (± 0.5) and 50% relative humidity. Creep tests were conducted to determine creep compliance, and creep-and-recovery tests were conducted to test linearity. A viscoelastic material is linear if and only if its response to stimulus satisfies the mathematical principles of homogeneity and superposition. These principles may be stated as:

Homogeneity:

$$\sigma_{ij}\{c\varepsilon_{kl}\} = c\sigma_{ij}\{\varepsilon_{kl}\} \quad (c = \text{constant}) \quad (1)$$

Superposition:

$$\sigma_{ij}\{\varepsilon_{kl}^a + \varepsilon_{kl}^b\} = \sigma_{ij}\{\varepsilon_{kl}^a\} + \sigma_{ij}\{\varepsilon_{kl}^b\} \quad (2)$$

where ε_{kl}^a and ε_{kl}^b may be either the same or different input histories and the braces are used to denote history-dependence. It is noted that satisfaction of superposition guarantees satisfaction of homogeneity, but that the converse statement is not true.⁷ An important consequence of this fact is that a creep-and-recovery test provides all that is needed to assess material linearity.

Creep tests were conducted on 12 specimens (**Table 1**). Five were loaded with 3.56 N, four with 8.01 N, and three with 12.45 N. These load levels are nominal (actual values varied somewhat from specimen to specimen due to factors such as variations in grips and extensometer spring forces). This resulted in nominal stresses within the test section of about 138, 310, and 490 kPa, respectively. Test duration ranged from a low of 70 to a high of 220 h.

The test procedure was as follows.

Table 1: Test matrix.

	Test 3	Test 4	Test 5	Test 6	Test 7
Station 1					
Specimen	4003-1	4004-1	4005-1	4006-1	4007-1
Creep load (N)	3.56	3.56	8.01	8.01	3.56
Thickness (cm)	0.1996	0.2017	0.1999	0.2108	0.2057
Width (cm)	1.2522	1.2649	1.2675	1.2548	1.2573
Creep stress (kPa)	142.4	139.5	316.1	302.8	137.7
Station 2					
Specimen	4003-2	4004-2	4005-2	4006-2	4007-2
Load (N)	8.01	8.01	8.01	8.01	8.01
Thickness (cm)	0.2022	0.1999	0.2019	0.2121	0.2070
Width (cm)	1.2675	1.2649	1.2624	1.2598	1.2598
Stress (kPa)	312.5	316.8	314.3	299.8	307.2
Station 3					
Specimen	4003-3	4004-3	4005-3	4006-3	4007-3
Load (N)	12.45	12.45	12.45	12.45	12.45
Thickness (cm)	0.2002	0.1991	0.2007	0.2090	0.2080
Width (cm)	1.2573	1.2522	1.2548	1.2598	1.2548
Stress (kPa)	494.6	499.4	494.4	472.8	477.0
Station 4					
Specimen	4003-4	4004-4	4005-4	4006-4	4007-4
Load (N)	3.56	3.56	3.56	3.56	3.56
Thickness (cm)	0.2007	0.1999	0.1976	0.2062	0.2080
Width (cm)	1.2598	1.2598	1.2548	1.2624	1.2649
Stress (kPa)	140.8	141.4	143.6	136.8	135.3

- Step 1.** Aluminum grips, with surfaces specially prepared to prevent slippage, were attached to one end of the specimen with threaded fasteners torqued to 2.03 J.
- Step 2.** The specimen was hung by the other end in a spring-loaded mechanical grip, and an extensometer was attached. A spring was attached to the extensometer to balance it so as to minimize the force imposed on the specimen by the extensometer.
- Step 3.** The specimen was left hanging overnight (generally about 16 h) with only the weight of the aluminum grips applied.
- Step 4.** The creep load was applied. This was accomplished by releasing a set screw which allowed the load (weights on a pan) to free-fall a short distance, thereby applying the load almost instantaneously.

As seen in **Fig. 3**, which shows the complete test set-up, a load cell is positioned at the top of the load train. Beneath the load cell is the mechanical grip, specimen (with extensometer attached), aluminum grip with slot to catch a ball attached to the weight

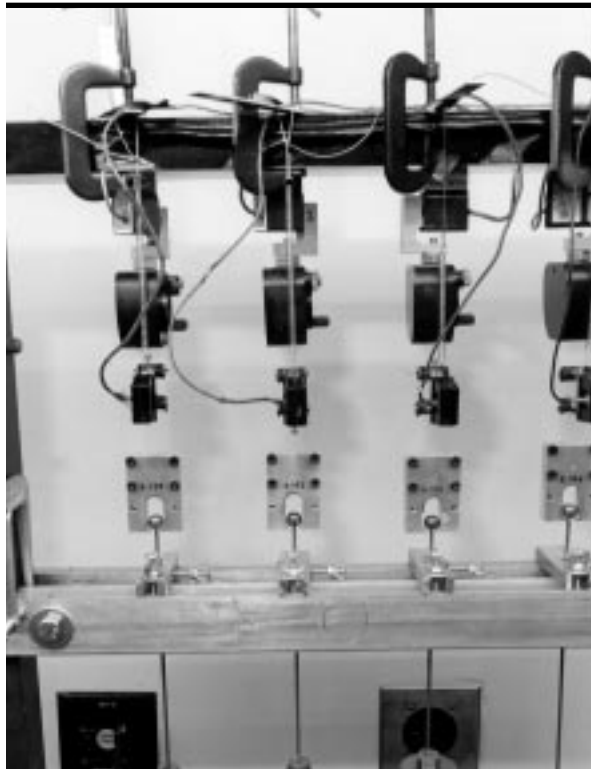


Figure 3. Test set-up.

pan when the pan is released, and finally, the weight pan. The specimens are difficult to see in **Fig. 3** because they are almost as clear as glass.

The load cells used were manufactured by Instron and were rated to 222.41 N (comparable load cells manufactured by Interface were used in Test 7 only). The extensometers, which were manufactured by Instron, had a 2.54-cm gage length and a +50% displacement range (except on station 4, where the displacement range was +10%). Four specimens were tested at a time.

The measured creep compliance, based on an average of the twelve test results, is presented in **Fig. 4**.

Ideally, a creep test involves the instantaneous application of a given load, P , at some time t_0 , to a previously unloaded specimen. The state of stress for $t \geq t_0$ is ideally spatially homogeneous and temporally constant. The creep tests conducted here deviate from the ideal in two respects: (1) the loading was not instantaneous, and (2) the specimens were not fully unloaded for $t < t_0$. The first deviation mentioned above is of little concern since the load was applied rapidly enough that the event was essentially instantaneous (especially for tests that ran several hours). The second deviation exists in large part as a consequence of the difficulty incurred in trying to apply the load instantaneously and, at the same time, obtain accurate measurement of strain.

Using spring-loaded mechanical grips at the bottom of the specimens was not practical since one could not attach them to the specimen and then release them in such a way as to approach a step input loading. Adding to the difficulty, one could not manually attach and release these mechanical grips without producing erroneous strain measurements (from jostling the specimen) at the instant of loading.

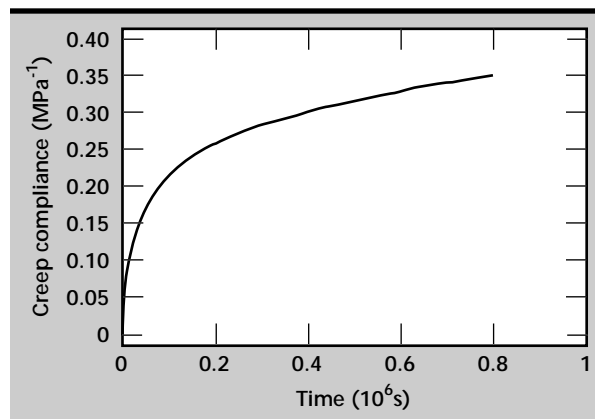


Figure 4. Creep compliance.

Hydraulic grips are encumbered by the same difficulties. The alternative chosen here, was to pre-load the specimen with the weight of the aluminum grips. This pre-loading took out any bending that may have been present due to the forces imposed by the extensometers and, at the same time, enabled the application of a load input that looks very much like a step function. By loading the specimens in this manner, we failed to satisfy the no-load for $t < t_0$ objective. We sought to minimize this deviation from the ideal by making the grips light (typically 0.88 N or less).

It is the opinion of the authors that the approach taken is justified on two counts: (1) fading memory serves to minimize the effects of the pre-loading; and (2) using a mechanical or hydraulic grip presents difficulties, as already mentioned.

Creep-and-recovery tests were conducted on eight specimens. Three were loaded (during the creep portion of the test) with 3.56 N, three with 8.01 N, and two with 12.45 N, nominally. The specimens were unloaded (except for the aluminum grips) during the recovery portion. Test procedures were identical to those described above for the creep tests, except that the load was removed after a given amount of time (generally about 50 h) to allow for recovery. This was accomplished by rapidly raising the weight pan a small amount and then tightening a set screw to hold it in place. The creep-and-recovery tests revealed the material to be linear under all three loading conditions.

DOC was measured by modulated DSC on selected specimens both before and after loading. All samples were found to be essentially amorphous, possessing 2% or less crystallinity.

Future Work

One obvious area for future work is testing Kel-F 800 at temperatures other than RT. It is possible that such testing will reveal the presence of a time/temperature superposition principle. This is all the more likely since the results of the current work revealed the material to be linear.

Another area for future work is to test at higher loads to determine the onset of nonlinearity.

A third topic for future study is to quantify the effect of DOC on creep compliance by conditioning specimens in such a way that creep compliance can be determined as a function of DOC.


A fourth area for future study is aging. It would be interesting to apply the methods of Struik⁸ to determine the effect of physical aging on creep compliance.

A fifth area for future work is the determination of the effect of specimen thickness. It may be that the properties of thin films of Kel-F 800 are not the same as the bulk properties.

Acknowledgments

The authors wish to express their thanks to M. Hoffman, C. Tarver, and J. LeMay for their involvement in initiating this work; to M. Hoffman for providing materials; to P. Harwood and S. Winchester for specimen fabrication; to B. Sanchez and R. Lum for conducting the mechanical tests; to G. Overturf for conducting the DSC; and to D. Lesuer for his overall support and guidance as Thrust Area Leader.

References

1. Cady, W. E., and L. E. Caley (1977), *Properties of Kel-F 800*, Lawrence Livermore National Laboratory, Livermore, Calif., (UCRL-52301).
2. Grotheer, E. W. (1988), *Characterization of PBX Binders*, Allied Signal, Kansas City, Mo., (BDX-613-3849).
3. Hoffman, D. M., F. M. Matthews, and C. O. Pruneda (1989), "Dynamic Mechanical and Thermal Analysis of Crystallinity Development in Kel-F 800 and TATB/Kel-F 800 Plastic Bonded Explosives. Part I Kel-F 800," *Thermochemica Acta*, Vol. **156**, (2), pp. 365-372.
4. Herold, R. D. (1990), *PBX Binders FY90-2*, Allied Signal, Kansas City, Mo, (KCP-613-4362).
5. Dobratz, B. M., and P. C. Crawford (1985), *LLNL Explosives Handbook, Change 2*, Lawrence Livermore National Laboratory, Livermore, Calif., (UCRL-52997).
6. Overturf III, G. E. and J. D. Lemay, (Draft), *Survey of Kel-F Literature for W87 LEP*, Lawrence Livermore National Laboratory, Livermore, Calif.
7. Schapery, R. A. (1974), "Viscoelastic Behavior and Analysis of Composite Materials," *Mechanics of Composite Materials*, G. P. Sendeckyj, Ed., Academic Press, New York, N.Y., pp. 85-168.
8. Struik, L. C. E. (1978), *Physical Aging in Amorphous Polymers and Other Materials*, Elsevier Scientific Publishing, Amsterdam, Netherlands. 



Technical Information Department
Lawrence Livermore National Laboratory
University of California
Livermore, California 94551